Supporting Information

Formation of a New Hydrated Sodium-Thorium Phosphate from Thorium Dioxide and its Subsequent Phase Evolution

Kramar B.V.,[a] Plakhova T.V.,[a] Kuzenkova A.S.,[a] Trigub A.L.,[a,b] Svetogorov R.D.,[a,b] Shiryaev A.A.[c], Nevolin I.M.,[a,c] Yapryntsev A.D.,[d] Baranchikov A.E.,[d] Peters G.,[b] Yapaskurt V.O.,[a] Egorov A.V.,[a] Kostyukov I.A.,[a] Shaulskaya M.D.,[a] Tsymbarenko D.M.,[a] Romanchuk A.Yu.,[a] and Kalmykov S.N. [a]

[a]Department of Chemistry, Lomonosov Moscow State University, Leninskie Gory 1/3, 119991 Moscow, Russia

[b]National Research Centre "Kurchatov Institute", 1, Akademika Kurchatova pl., 123182 Moscow, Russia

[c]Frumkin Institute of Physical Chemistry and Electrochemistry, Russian Academy of Sciences, Leninsky Prospect 31 bld. 4, 119071 Moscow, Russia.

[d]Kurnakov Institute of General and Inorganic Chemistry of the Russian Academy of Sciences, Leninsky Prospect 31, 117901 Moscow, Russia

Contents

List of Figures

Section S1. Hydrothermal Synthesis

Table S1. The pH values recorded for the buffer and synthetic mixture before and after synthesis.

Sample	pH (buffer)	pH (before HT)	pH (after HT)
ThPhos-5	4.8	5.47	5.45
ThPhos-5-Na	4.8	5.33	5.49
ThPhos-7	6.4	6.85	7.1
ThPhos-8	7.5	8.77	10.23

The equation for the reforming of amorphous ThO_2 is hypothesized to follow Eqn. S1 or Eqn. S2 depending on acidobasic properties of the medium:

$2ThO_2 + Na^+ + 3PO_4^{3-} + 8H^+ \rightarrow NaTh_2(PO_4)_3 + 4H_2O$ (Eqn. S1)

$2ThO_2 + Na^+ + 3PO_4^{3-} + 4H_2O \rightarrow NaTh_2(PO_4)_3 + 8OH^-$ (Eqn. S2)

i.e. the increase in pH when the thorium oxide is reformed into the phosphate is not surprising.

Section S2. Additional TEM Data

This section presents additional representative images taken on samples ThPhos-5 and ThPhos-8, as well as the TEM-EDS data. These images were not filtered or denoised. In light of the high degree of particle overlap, as observed in these images, we opted against trying to rigorously quantify the average particle size from TEM.

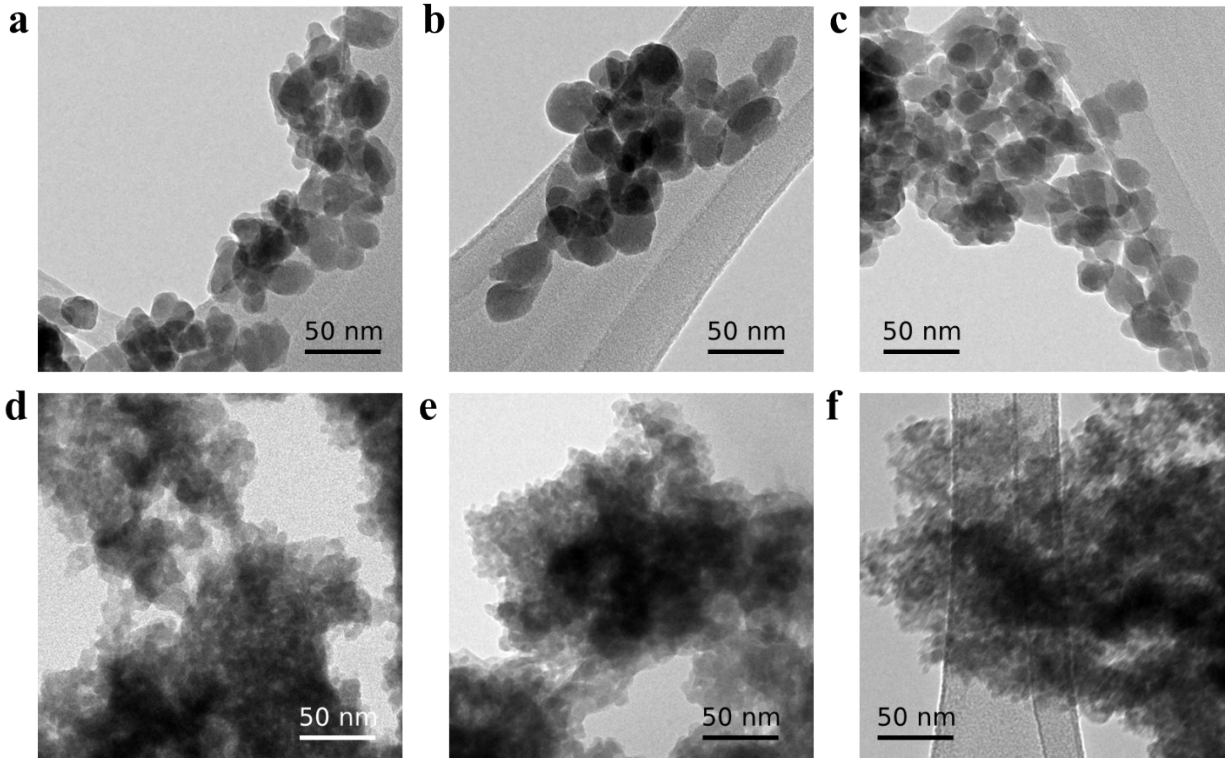

Figure S1. TEM micrographs of samples ThPhos-5 (a-c) and ThPhos-8 (d-f)

Table S2. Averaged results of elemental analysis (atomic %) via EDS for samples ThPhos-5 and ThPhos-8

Element	Sample ThPhos-5 (atomic %)	Sample ThPhos-8 (atomic %)
Na	7 ± 1.2	12 ± 3.2
Th	17.2 ± 0.62	21 ± 1.8
P	13 ± 1.1	11 ± 1.1
O	63 ± 1	55 ± 3

Section S3: X-ray Diffraction Pattern Comparison and Literature Screening

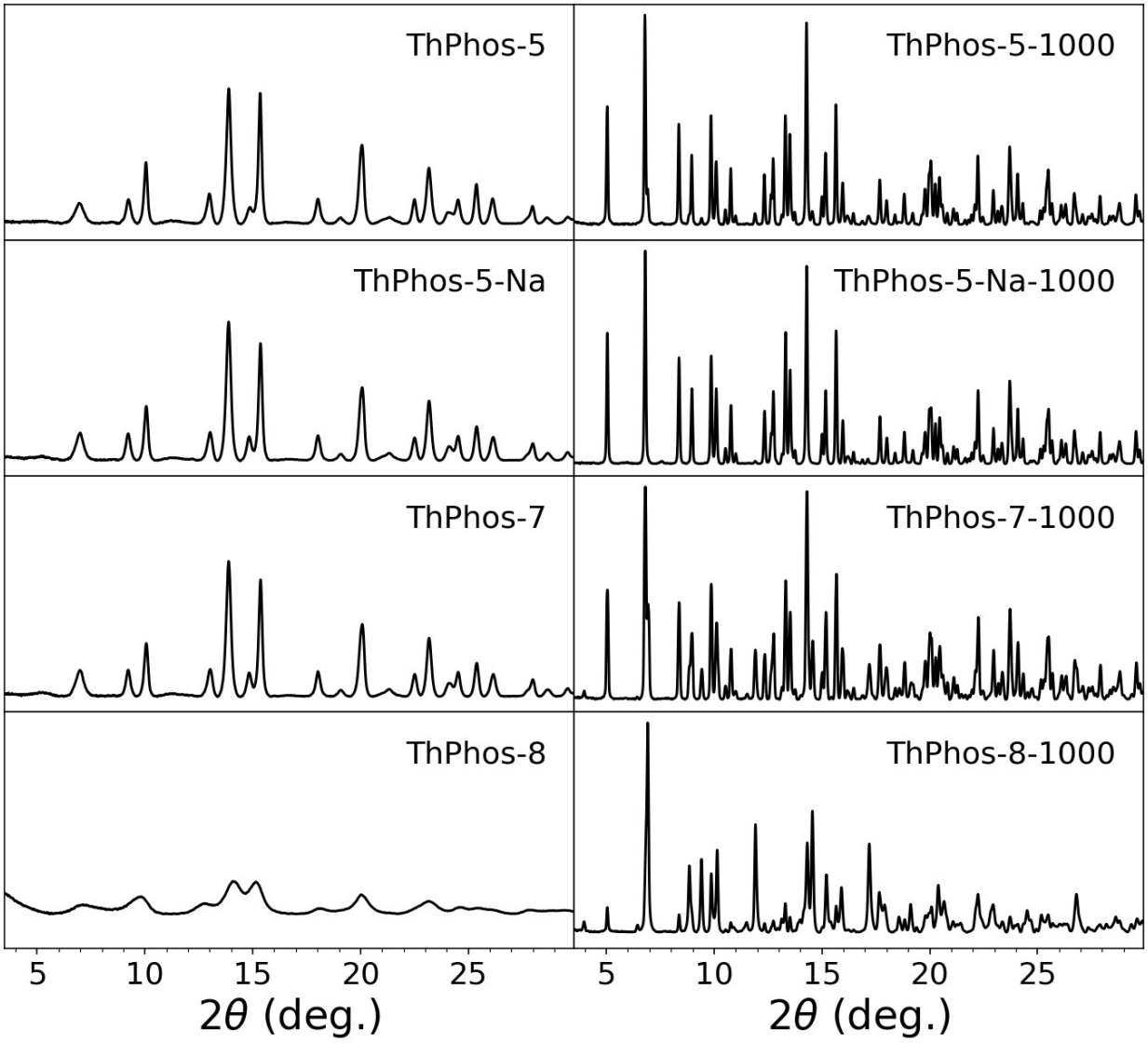

Figure S2. Side-by-side comparison of the hydrothermally obtained products against the calcined samples.

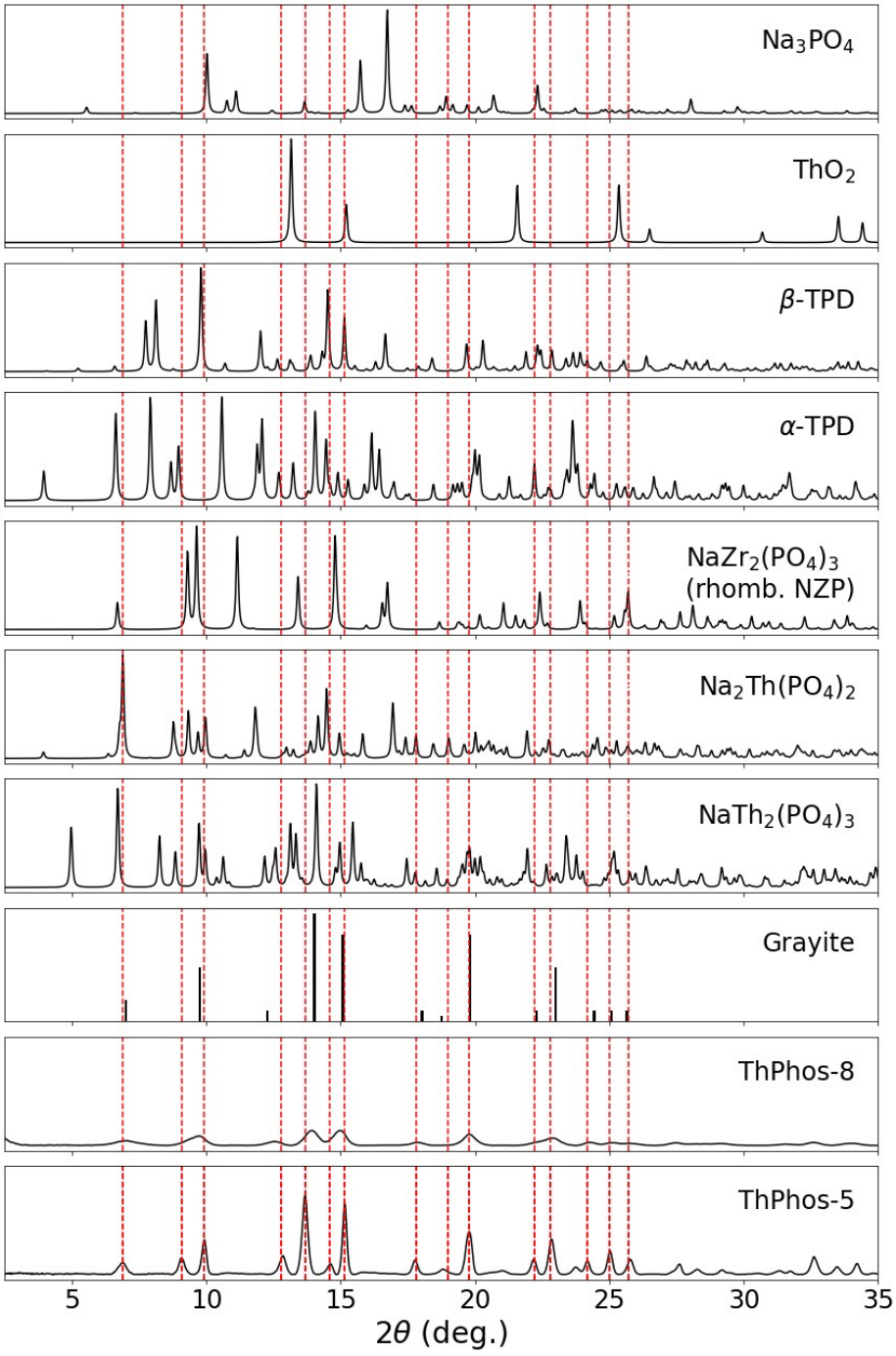

Figure S3. Comparison of the powder X-ray diffraction pattern of samples ThPhos-5 and ThPhos-8 versus relevant crystalline phases from the literature.[1–6] The grayite structure was reproduced from the PDF 4+ database (#00-042-1389). Red dashed lines added to aid in visual matching to sample ThPhos-5. All patterns are plotted in accordance with a 0.74 Å X-ray probe wavelength.

Section S4: Small-Angle X-ray Scattering

Fitting of the SAXS data was carried out by two different models: Unified and an extended version of the Guinier-Porod model.[7–9] Both models are empirical in nature and are commonly used to describe small angle scattering from hierarchically structured samples. They achieve this by incorporating multiple Guinier and Porod regions and ensuring a smooth transition between them. Usage of such models requires that the experimental q-range spans at least a few orders of magnitude.

In the case of the Unified model, the function supplied with SasView software was used without any further modification. It effectively modeled the q-range from about 0.007 to about 0.5 $Å^{-1}$ (Fig. S3a-b), capturing two obvious Guinier-like shoulders on the double logarithmic plot for both samples.

In the case of the Guinier-Porod model, the implementation in SasView was modified to span two Guinier regions and one Porod region, i.e. Guinier-Guinier-Porod, **GGP**.[9] Described below, this function was better at fitting low q values and worse at fitting high q, notably being insufficient to capture the lower Guinier-like shoulder on the double logarithmic plot (S3b-c).

The equations take the following form:

$I(q) =$ (Eq. 1.1, 1.2 and 1.3)

where:

The fitting parameters are G_1, which is taken care of by the SasView default parameter *scale*; dimensionalities s_1 and s_2 ($3 > s_1 > s_2$); Porod exponent d; and radii of gyration R_{g1} and R_{g2}. The values Q_1 and Q_2 are determined during the fit from the aforementioned fitting parameters; these values also define the switching points between the different Guinier and Porod regions. The scaling factor D, which adjusts intensity in the Porod region, is also calculated from the other fitting parameters. The parameter R_{g2} corresponds to the larger particle dimension. The best-fit parameters obtained with the GGP model corresponded to cylindrical morphology for the primary particle ($s_1 \sim 1$, $s_2 \sim 0$). The radii of gyration were used to calculate rod length and thickness by equations 6 and 7:

$$R_{g2} = \sqrt{\left(\frac{L^2}{12} + \frac{R^2}{2}\right)} \qquad \text{(Eq. 6)}$$

$$R_{g1} = R/\sqrt{2} \qquad \text{(Eq. 7)}$$

Neither function described the complex high-q features observed for ThPhos-5 and ThPhos-8 alike near 1 $Å^{-1}$. We did not assign those features. Both functions also fail to capture the low-q tail of the data, which,

however, is well-described by a simple power law, which stems from the presence of larger aggregates beyond the experimental limit.

The grain size in sample ThPhos-5-1000 precluded quantitative SAXS analysis of particle size. The data collected for ThPhos-5-1000 was only fit to a simple power law to characterize the Porod (surface) scattering. Notably, a value under 4 typically indicates a surface fractal system,[10] which is the case here (Fig. S3e).

No SAXS data was collected for ThPhos-8-1000. As seen from the SEM micrographs collected for ThPhos-8-1000, the grain size in that sample was not sufficiently small for characterization via SAXS, as in the case of ThPhos-5-1000.

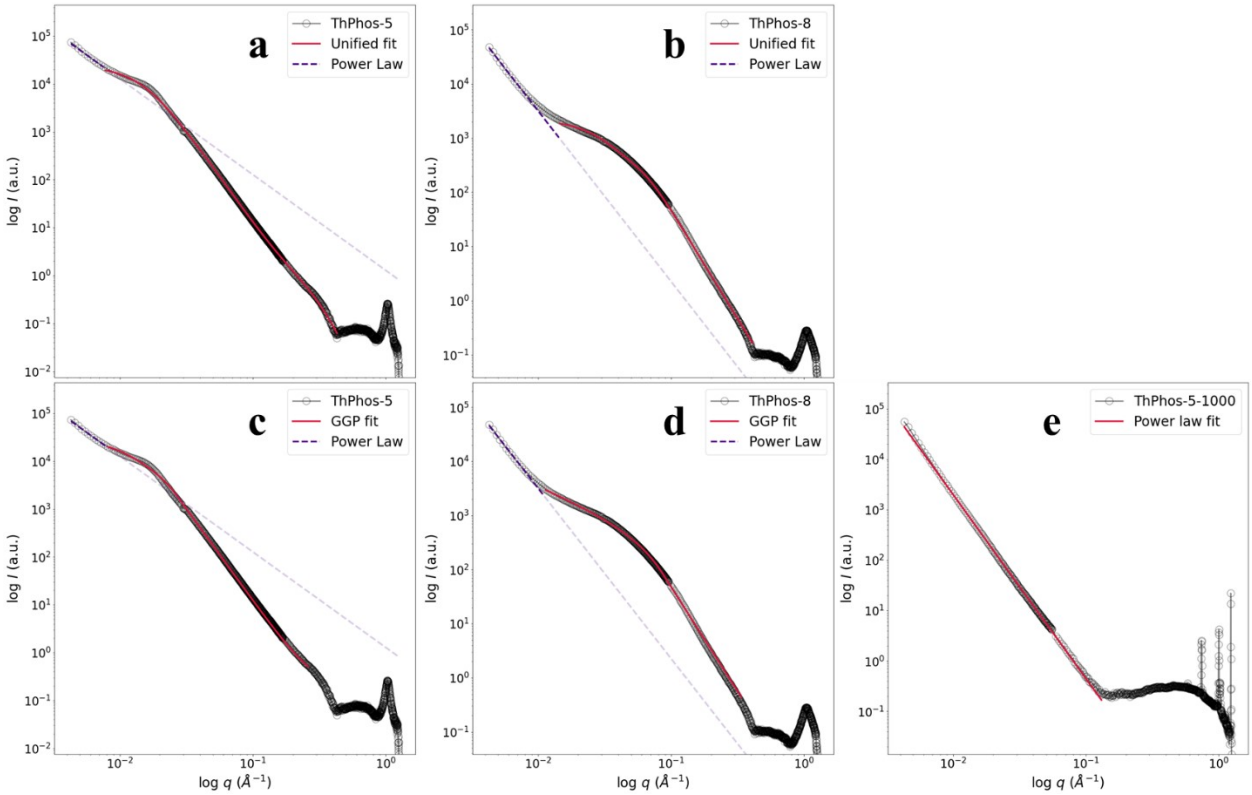

Figure S4. The unnormalized SAXS data plotted on double logarithmic axes for (a,c) ThPhos-5, (b,d) ThPhos-8 and (e) ThPhos-5-1000. The experimental datasets are plotted in black circles. Red lines indicate the primary fit with the (a,b) Unified model, (c,d) GGP model or (e) power law model. Indigo dashed lines in panels (a-d) indicate an auxiliary power law fit in the low-q region. The changes in data point density, observed for all datasets at different q-values, are caused by the data being stitched after having been taken on two different sample-detector distances.

Table S3. Best fit parameters for the SAXS data.

Model	Parameter	ThPhos-5	ThPhos-8	ThPhos-5-1000
GGP	**s** s_1**1**	0.955	1.10	-
	s_2	0	0.0933	-
	d	3.92	3.76	-
	R_{g1} ($Å^{-1}$)	63.109(2)	18.526(9)	-
	R_{g2} ($Å^{-1}$)	134.84(0)	114.7	-
Unified	d_1	4.00	4.00	-
	d_2	3.89	4.00	-
	R_{g1} ($Å^{-1}$)	7.95	10.2	-
	R_{g2} ($Å^{-1}$)	122	55.9	-
	G_1	0.0014	0.0108	-
	G_2	39.718	6640.5	-
	B_1	1.0E-6	4.5E-6	-
	B_2	2.4E-6	0.0133	-
Power Law	B_1	1.0E-6	4.5E-6	-
	B_2	2.4E-6	0.0133	-
	α	2.00	3.15	3.65

Section S5. Scanning electron microscopy and energy dispersive X-ray spectroscopy

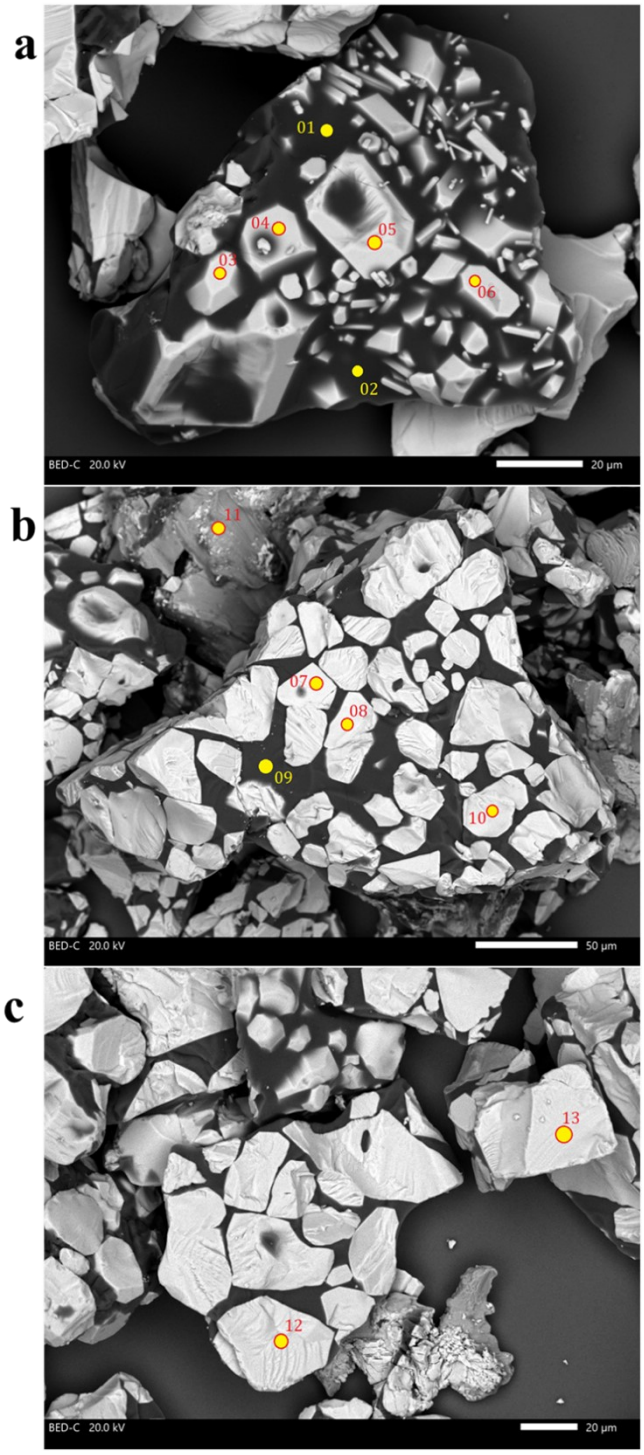

Figure S5. SEM images of sample ThPhos-5-1000. Marked and labeled are the approximate positions where EDS measurements were taken: yellow circled in red (crystallites), or flat yellow (matrix, morphologically amorphous sections).

For 7 points, the results of the elemental analysis were consistent with the expected composition of $NaTh_2(PO_4)_3$ (see Table S2). Analysis of the other 6 points revealed the presence of impurities in the sample. No attempt was made to precisely characterize the composition and structure of these impurities. A thorough review of experimental procedure allowed us to conclude that residual aluminum was likely deposited into the crucible when sample ThPhos-5 was transferred before the calcination; and the most likely cause for the presence of steel is that post-calcination the sample ThPhos-5-1000 was scraped out with a metal spatula. These conclusions are corroborated by the fact that SEM-EDS for Sample ThPhos-8-1000 did not reveal the presence of aluminum or any other extraneous elements in significant quantities (Fig. S5, Table S3).

Table S4. EDS results (atomic %) for the points marked on the SEM images in Fig. S4.

Point ID	O %	Na %	Al %	P %	Th %
3	69.73	5.34	0	14.64	10.3
6	72.25	5.47	0	13.44	8.83
7	71.3	3.52	0	14.91	10.27
8	70.59	4.97	0	14.44	10
10	72.4	5.2	0	13.3	9.1
12	69.53	4.9	0	14.86	10.71
13	70.4	5.21	0	14.41	9.98
Average	70.89	4.94	0.00	14.29	9.88
Expected for $NaTh_2(PO_4)_3$	66.67	5.56	-	16.67	11.11
		Impurity 1: Al-containing sodium-thorium phosphate			
Point ID	O %	Na %	Al %	P %	Th %
4	70.86	8.16	1.49	12.14	7.36
5	71.22	7.11	1.39	12.52	7.77
Average	71.04	7.635	1.44	12.33	7.565
		Impurity 2: Amorphous double sodium-aluminum phosphate			
Point ID	O %	Na %	Al %	P %	(Si, Ca, Ti, Mo, Th) %
1	62.67	17.57	8.54	10.58	0.65
2	57.89	15.54	10.73	14.62	1.22
9	60.23	17.95	9.15	12.28	0.38
Average	60.26	17.02	9.47	12.49	0.75
		Impurity 3: Steel			
Point ID	O %	Na %	Cr %	Fe %	Ni %	(Al, Si, P, Mn, Nb, Th) %
11	13.90	5.09	15.69	52.16	7.14	~6 %

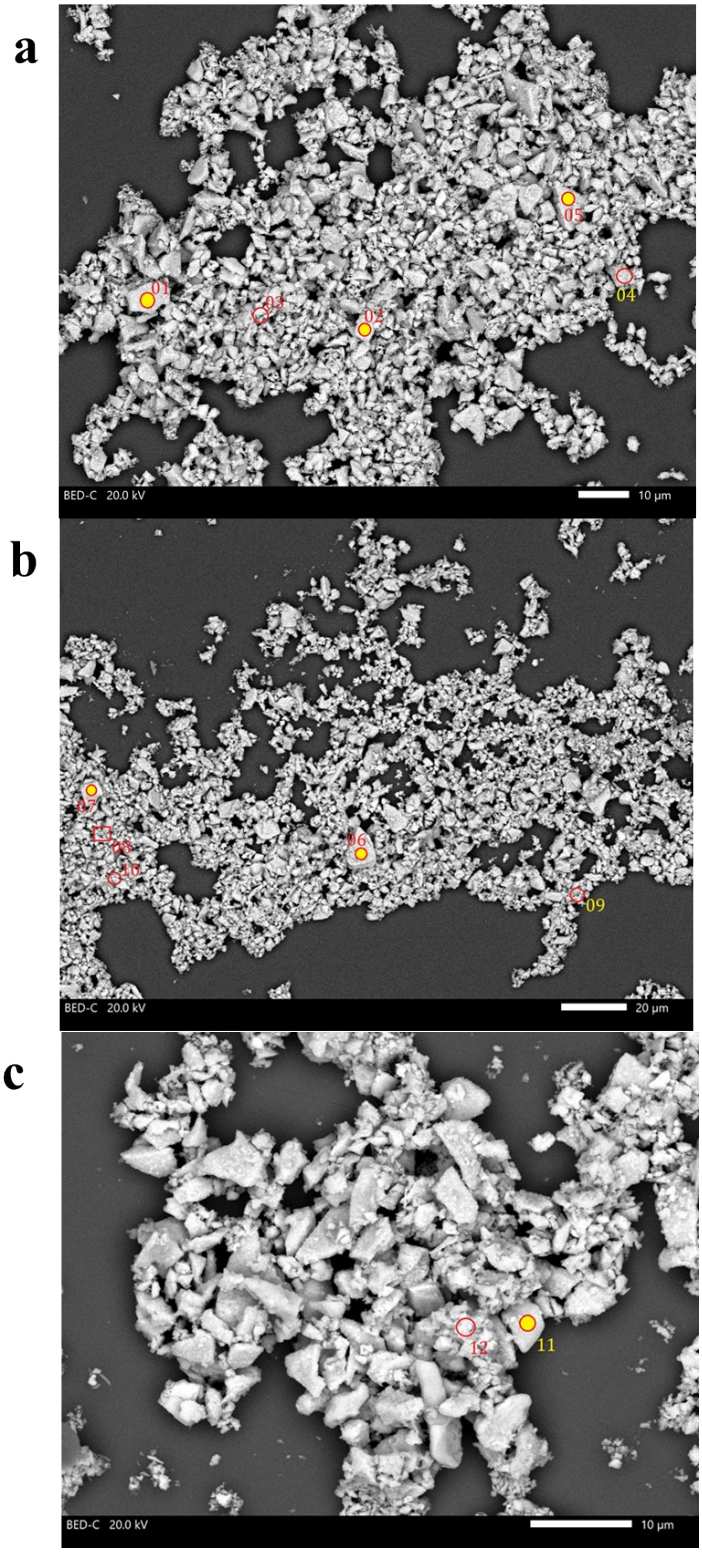

Figure S6. SEM images of sample ThPhos-8-1000. Marked and labeled are the approximate positions where EDS measurements were taken: colorless red circles (multiple crystallites), or yellow circled in red (larger crystallites).

Examination of the EDS results for the points marked in Fig. S5 shows that the sample ThPhos-8-1000 does not appear to contain major impurities. The origin of residual Si and Al recorded for point 4 are unknown; it is likely that these elements could get on the sample during experimental preparation for SEM-EDS. The elemental ratios are quite close to the expected ones, but not exactly there.

Table S5. EDS results (atomic %) for the points marked on the SEM images in Fig. S5.

Point ID	O %	Na %	Al %	Si %	P %	Th %
1	65.53	12.02	-	-	14.35	8.11
2	66.11	11.56	-	-	14.21	8.12
3	67.4	14.38	-	-	12.13	6.08
4	65.65	12.5	1.23	1.77	12.67	6.19
5	64.96	12.72	-	-	14.25	8.07
6	60.13	11.37	-	-	17.42	11.08
7	64.31	14.27	-	-	13.96	7.46
8	64.1	12.13	-	-	14.59	9.19
9	67.93	11.95	-	-	12.88	7.24
10	64.26	11.22	-	-	14.97	9.55
11	67.07	14.03	-	-	12.54	6.36
12	65.77	12.21	-	-	13.87	8.15
Average	65.27	12.53			13.99	7.97
Expected for $Na_2Th(PO_4)_2$	61.54	15.38	-	-	15.38	7.69

Section S6. In-situ high temperature XRD

The temperature-vs-time profile for the two HT XRD experiments are plotted below.

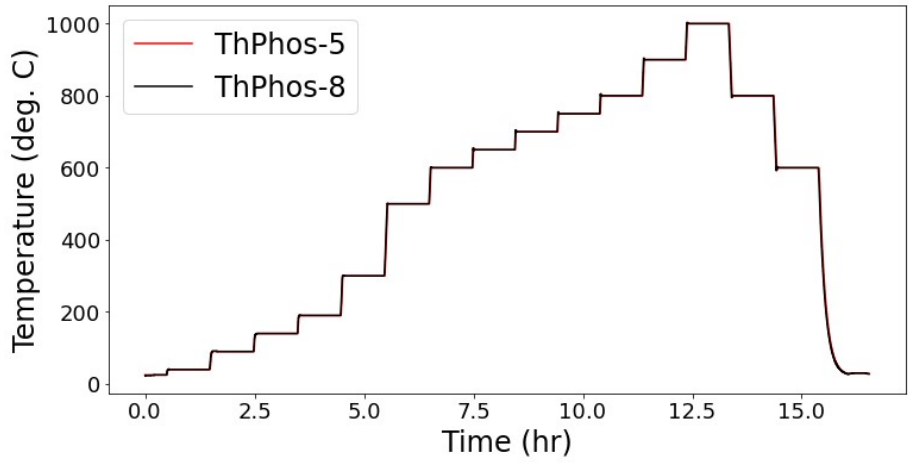

Figure S7. Heating profiles for samples ThPhos-5 and ThPhos-8.

The data plotted on Fig. 2a and 2b in the main paper can be alternatively displayed in a pseudo-3D representation (Fig. S7, some temperature points omitted for clarity).

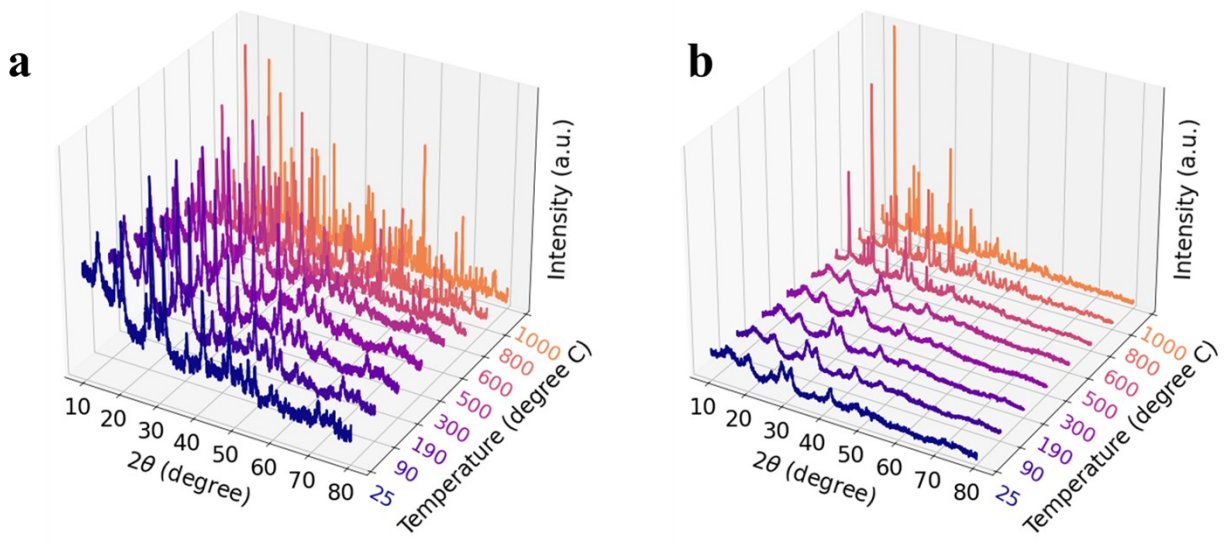

Figure S8. High temperature XRD data for ThPhos-5 (a) and ThPhos-8 (b), in a pseudo-3D representation.

Section S7. PXRD and Rietveld Refinement

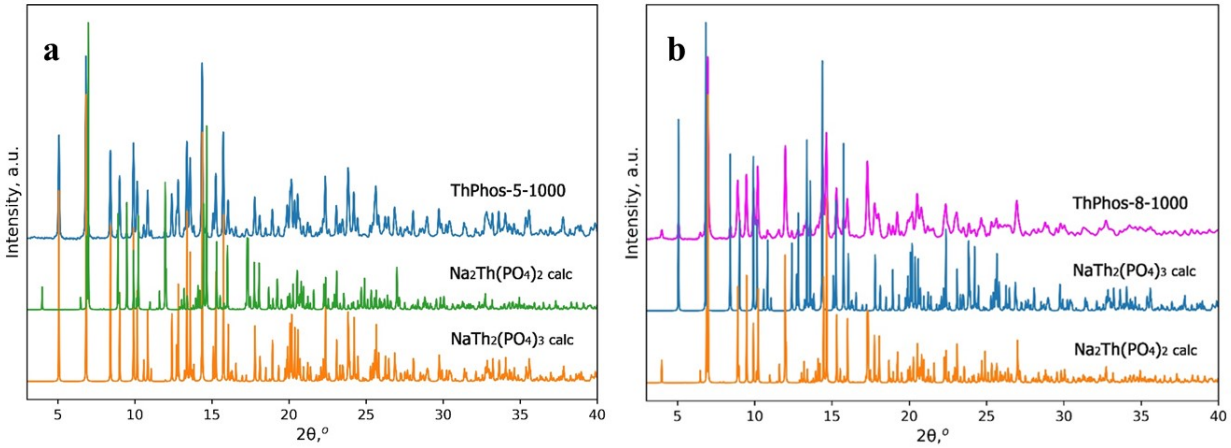

Figure S9. (a) Experimental PXRD of ThPhos-5-1000 and calculated PXRD of phases $NaTh_2(PO_4)_3$ and $Na_2Th(PO_4)_2$ (λ= 0.754 Å). The presence of reflections of both phases is observed in the experimental PXRD. (b) Experimental PXRD of ThPhos-8-1000 and calculated PXRD of phases $Na_2Th(PO_4)_2$ and $NaTh_2(PO_4)_3$ (λ= 0.754 Å). The presence of reflections of both phases is observed in the experimental PXRD.

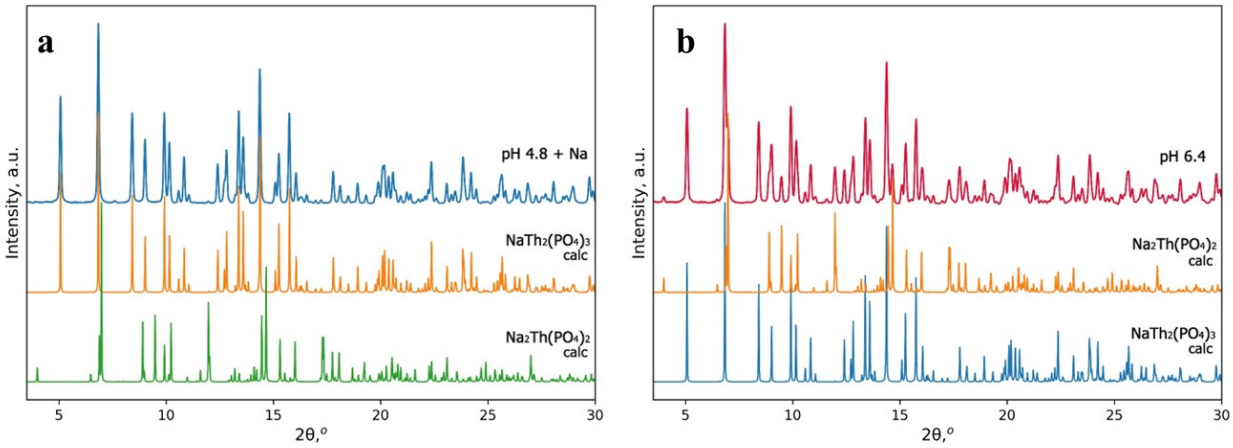

Figure S10. (a) Experimental PXRD of ThPhos-5-Na-1000 and calculated PXRD of phases $NaTh_2(PO_4)_3$ and $Na_2Th(PO_4)_2$ (λ= 0.754 Å). Only the $NaTh_2(PO_4)_3$ phase is observed. (b) Experimental PXRD of ThPhos-7-1000 and calculated PXRD of phases $Na_2Th(PO_4)_2$ and $NaTh_2(PO_4)_3$ (λ= 0.754 Å). The presence of reflections of both phases is observed in the experimental PXRD.

Rietveld refinements of XRD patterns of ThPhos-5-1000 and ThPhos-8-1000 samples after calcination at 1000ºC were performed to confirm the phase composition and elaborate the phase fraction. Both samples were fitted as two-phase mixture of $NaTh_2(PO_4)_3$ and $Na_2Th(PO_4)_2$. Pseudo-Voight peak profile function parameters (GW and LY), 8-10 term of Legendre polynomials background, unit cell parameters and phase fractions as well as atomic positions (for all atoms in $NaTh_2(PO_4)_3$ and for Th atoms in $Na_2Th(PO_4)_2$) were refined (Tables S5-S7).

Table S6. Results of two-phase Rietveld refinements against PXRD data of ThPhos-5-1000 and ThPhos-8-1000 samples. The major components are highlighted in bold.

Parameter	ThPhos-5-1000		ThPhos-8-1000	
Phase	**$NaTh_2(PO_4)_3$**	$Na_2Th(PO_4)_2$	$NaTh_2(PO_4)_3$	**$Na_2Th(PO_4)_2$**
Space group	*C2/c*	*$P2_1/c$*	*C2/c*	*$P2_1/c$*
a, Å	17.36485(19)	7.0691(11)	17.3423(19)	7.0644(2)
b, Å	6.81525(7)	21.688(4)	6.8085(7)	21.6771(9)
c, Å	8.13895(9)	9.1154(18)	8.1391(10)	9.1285(4)
β, °	100.9290(10)	111.686(19)	100.989(9)	111.768(4)
V, Å^3	945.741(13)	1298.60(3)	943.40(11)	1298.23(6)
Phase amount, wt.%	**87.1(3)**	12.9(3)	14.9(2)	**85.1(2)**
LY / $LY_{(001)}$	0.108(3) / 0.064(4)	0.49(3)	0.258(16)	0.417(8)
GW	0.1132(8)		0.143(3)	
Goodness of fit	0.34		0.74	
Rp / ωRp, %	0.92/1.25		1.24/1.89	
R_1, ωR_2	2.69 /3.32	2.75/2.90	3.67/4.39	3.49 /4.20

Table S7. Atomic positions of $NaTh_2(PO_4)_3$ phase after Rietveld refinement against PXRD data of ThPhos-5-1000 sample.

Atom	x	y	z	Uiso
Th1	0.15303(6)	0.09213(14)	0.03651(12)	0.0057
P1	0.3117(3)	0.0858(11)	0.3101(6)	0.0089
O3	0.2271(3)	0.0445(14)	0.33	0.0063
O4	0.3634(6)	-0.0982(12)	0.3428(11)	0.0114
O5	0.2947(6)	0.1460(14)	0.1246(8)	0.0063
O6	0.3520(8)	0.2538(13)	0.4200(12)	0.0114
P2	0	0.0995(15)	-0.25	0.0132
Na1	-0.0264(13)	0.597(4)	-0.371(2)	0.1127
O1	-0.0732(5)	-0.0255(12)	-0.2442(12)	0.0114
O2	0.0192(7)	0.2228(14)	-0.0895(12)	0.0165

Table S8. Atomic positions of $Na_2Th(PO_4)_2$ phase after Rietveld refinement against PXRD data of ThPhos-8-1000 sample. Only positions of Th1 and Th2 atoms were refined due to strong correlation of other parameters.

Atom	x	y	z	Uiso
Th1	0.2623(15)	0.17915(17)	0.2426(13)	0.0092
Th2	0.251(2)	-0.04570(15)	0.2471(18)	0.0112
P1	-0.072	0.0630	0.1470	0.011
P2	0.5704	0.0596	0.3488	0.011
P3	0.0716	0.3165	0.3697	0.011
P4	0.4436	0.3153	0.1182	0.012
Na1	-0.365	0.1871	0.0067	0.031
Na2	-0.124	0.1869	0.4776	0.036
Na3	0.1457	0.4376	0.0442	0.029
Na4	0.3582	0.4394	0.4531	0.030
O1	-0.276	0.0630	0.0057	0.016
O2	0.7686	0.0591	0.4912	0.021
O3	0.1011	0.0570	0.0813	0.025
O4	0.386	0.0552	0.4055	0.026
O5	-0.042	0.1214	0.2429	0.017
O6	0.5461	0.1176	0.2503	0.016
O7	-0.051	0.0053	0.2516	0.015
O8	0.5501	0.0014	0.2476	0.016
O9	0.2879	0.3312	0.4775	0.018
O10	0.2227	0.3300	0.0107	0.017
O11	-0.039	0.3030	0.4834	0.017
O12	0.5498	0.3017	0.0022	0.019
O13	-0.014	0.3740	0.2662	0.022
O14	0.5348	0.3712	0.223	0.018
O15	0.0561	0.2617	0.2621	0.019
O16	0.4588	0.2591	0.2247	0.019

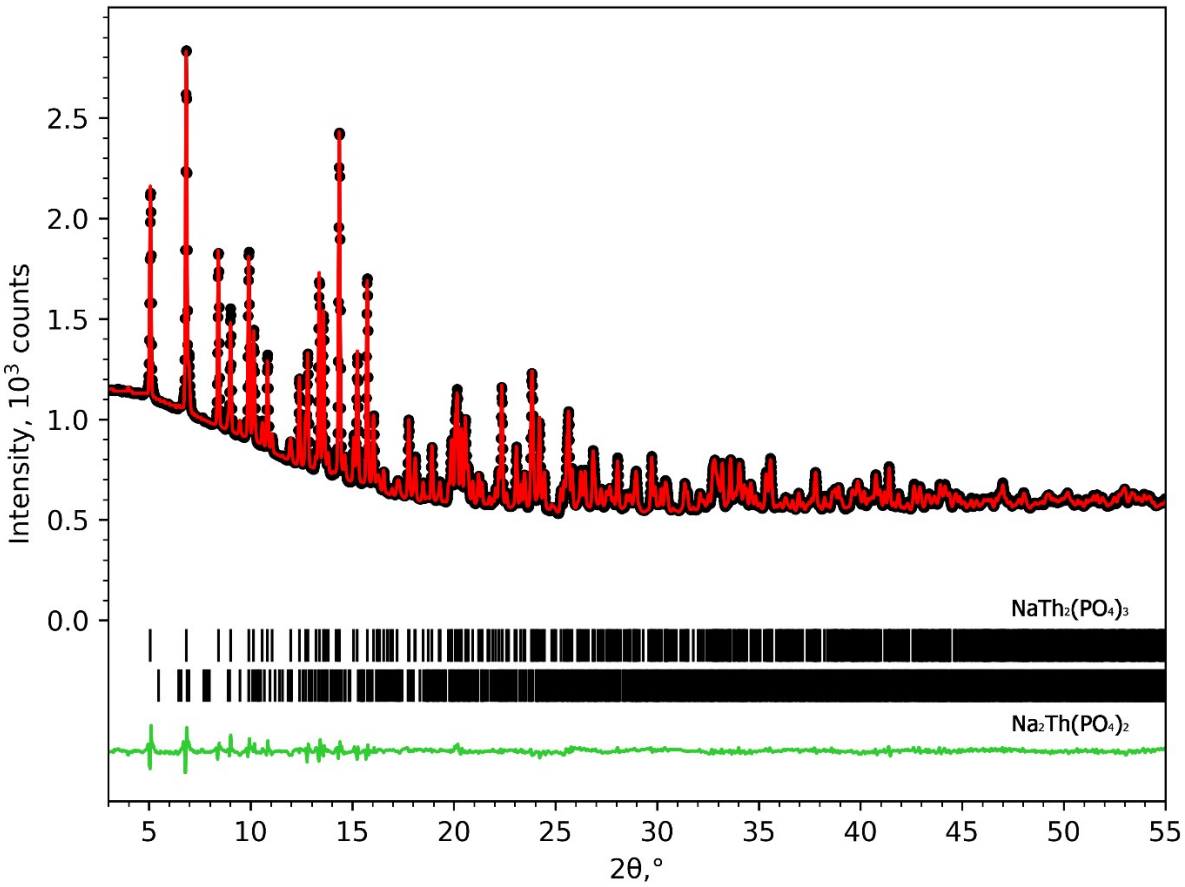

Figure S11. Rietveld refinement plot (λ= 0.754 Å) of the powder XRD pattern of ThPhos-5-1000. The ThPhos-5-1000 phase is a mixture of phases $NaTh_2(PO_4)_3$ and $Na_2Th(PO_4)_2$ with the weight fraction of 0.871(3) and 0.129(3), respectively, as established from the present refinement. Experimental data (black markers), refinement fit (red solid line), difference profile (offset green line), and positions of Bragg peaks (vertical bars).

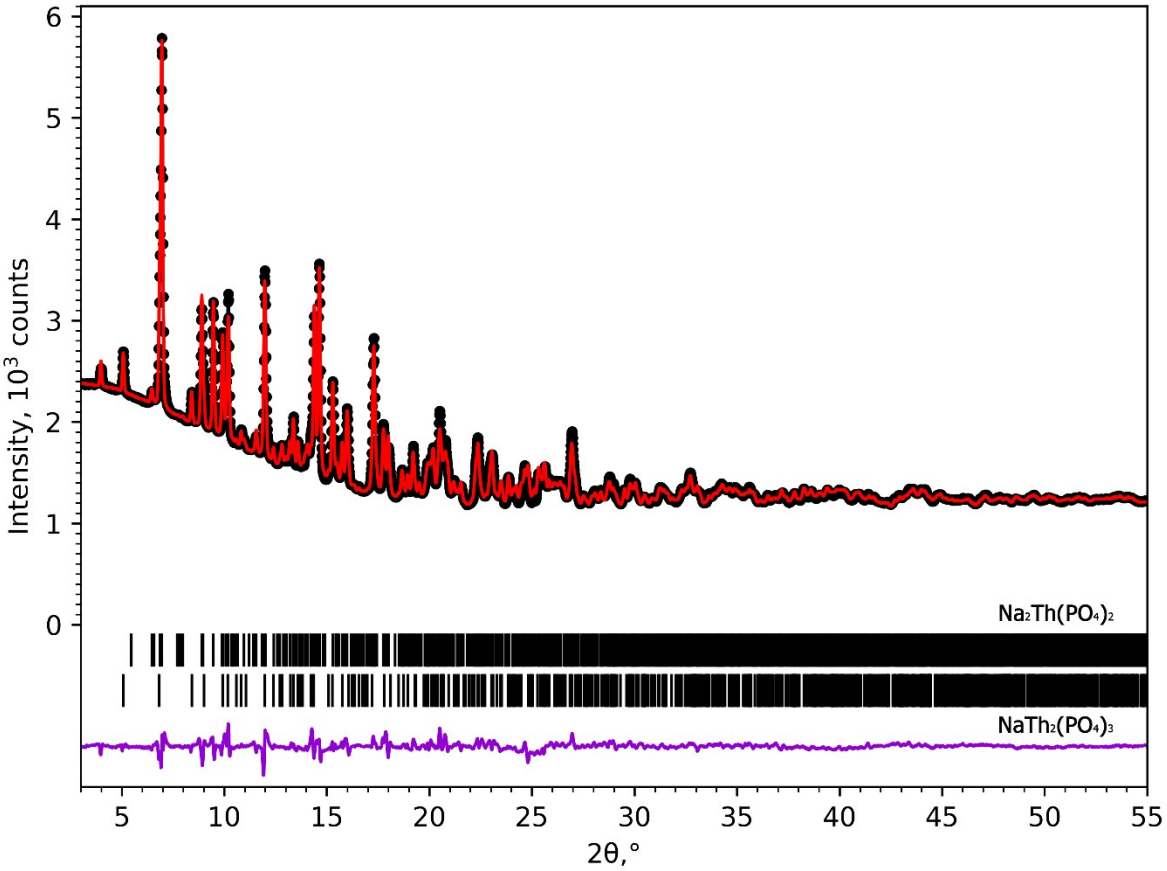

Figure S12. Rietveld refinement plot (λ= 0.754 Å) of the powder XRD pattern of ThPhos-8-1000. The ThPhos-8-1000 phase is a mixture of phases $Na_2Th(PO_4)_2$ and $NaTh_2(PO_4)_3$ with the weight fraction of 0.851(2) and 0.149(2), respectively, as established from the present refinement. Experimental data (black markers), refinement fit (red solid line), difference profile (offset purple line), and positions of Bragg peaks (vertical bars).

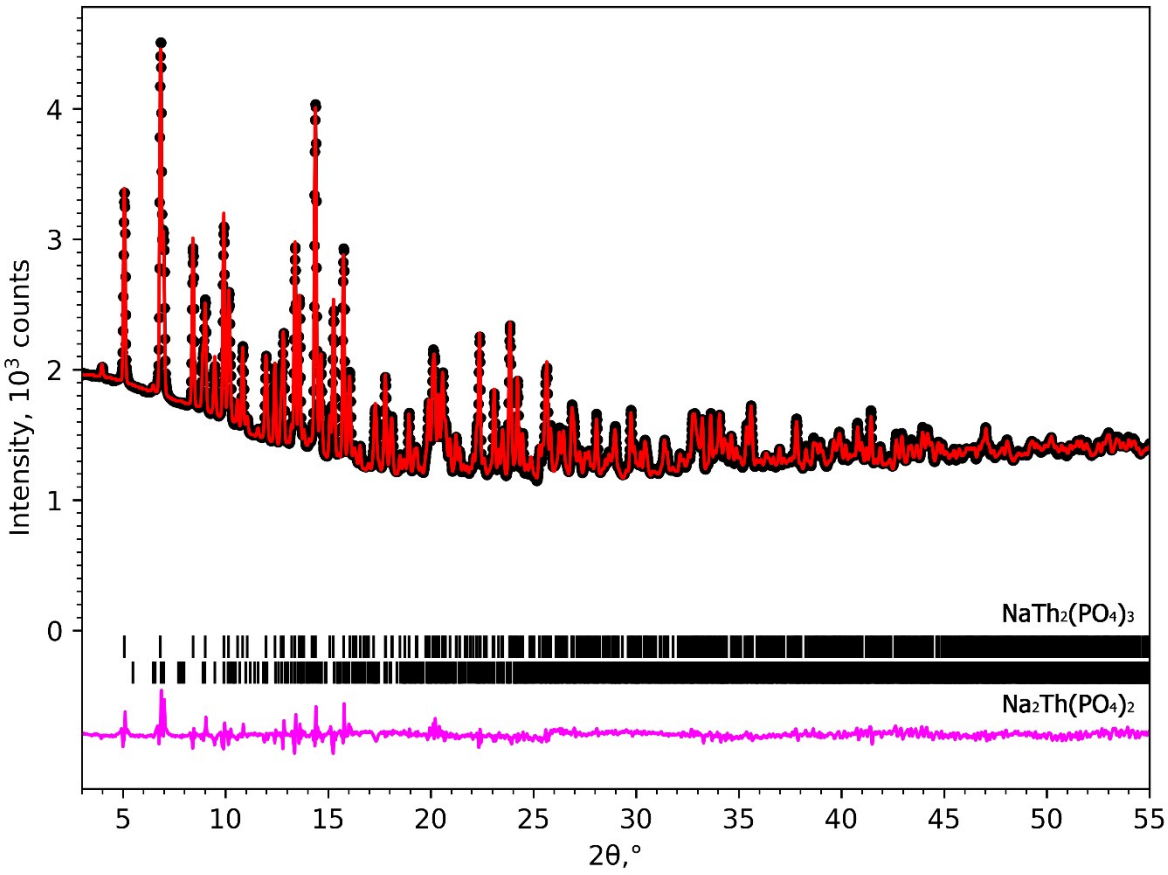

Figure S13. Rietveld refinement plot (λ= 0.754 Å) of the powder XRD pattern of ThPhos-7-1000. The ThPhos-7-1000 phase is a mixture of phases $NaTh_2(PO_4)_3$ and $Na_2Th(PO_4)_2$ with the weight fraction of 0.675(2) and 0.325(2), respectively, as established from the present refinement. Experimental data (black markers), refinement fit (red solid line), difference profile (offset purple line), and positions of Bragg peaks (vertical bars).

Section S8. Pair distribution function analysis

Table S9. Pearson correlation coefficients (r) values describing the relationship between experimental PDF data for ThPhos-5 and ThPhos-8, and the theoretical PDF data for Zr-P-O, Zr-As-O, Ce-P-O, Ce-As-O, Th-P-O, Th-As-O compounds from ICSD database. Correlations were calculated over the distance range 1-15 Å.

Composition	ICSD number	r for ThPhos-5	r for ThPhos-8
Th-P-O	1536395	0.8114	0.8211
Th-P-O	30432	0.8355	0.8057
Th-P-O	154632	0.7877	0.7260
Ce-P-O	31563	0.7078	0.7258
Ce-P-O	27860	0.7316	0.7004
Th-P-O	154633	0.6713	0.5825
Ce-As-O	95334	0.4949	0.5293
Th-As-O	1654737	0.4897	0.5241
Th-As-O	1689931	0.4805	0.5172
Zr-As-O	1728807	0.4466	0.5009
Ce-P-O	65193	0.3851	0.4980
Ce-As-O	1650371	0.4036	0.4758
Ce-P-O	429910	0.3961	0.4561
Th-As-O	1717091	0.4766	0.4406
Th-P-O	80863	0.3264	0.4227
Th-As-O	1717090	0.4547	0.4151
Th-P-O	60114	0.3272	0.4109
Th-P-O	201880	0.3134	0.4019
Ce-As-O	291399	0.3932	0.4007
Ce-As-O	426720	0.3926	0.4002
Ce-As-O	1732947	0.3932	0.3998
Ce-As-O	54879	0.4878	0.3996
Th-P-O	291100	0.3836	0.3969
Th-P-O	32522	0.3657	0.3905
Zr-P-O	61155	0.3587	0.3855
Ce-As-O	166938	0.4010	0.3714
Ce-As-O	1704106	0.2833	0.3647
Th-P-O	417156	0.3271	0.3575
Th-As-O	1717092	0.4327	0.3476
Ce-As-O	1704107	0.2507	0.3387
Ce-As-O	280982	0.3962	0.3271
Ce-As-O	166936	0.2170	0.3254
Ce-As-O	166935	0.3843	0.3225
Th-P-O	23734	0.3412	0.3207
Ce-P-O	421725	0.2607	0.3163
Th-As-O	1717093	0.2829	0.2959
Ce-P-O	416615	0.2624	0.2875
Ce-P-O	20737	0.2604	0.2829
Ce-P-O	416475	0.2982	0.2661
Ce-P-O	425082	0.2559	0.2598
Ce-As-O	1648018	0.2198	0.2478

Ce-P-O	154075	0.2342	0.2376
Ce-As-O	1697956	0.1475	0.2294
Zr-P-O	183237	0.2351	0.2148
Ce-P-O	49510	0.2203	0.2141
Ce-P-O	165876	0.2690	0.2078
Ce-As-O	1691977	0.1416	0.2035
Zr-P-O	65704	0.1897	0.2020
Ce-As-O	1689286	0.1372	0.2005
Ce-As-O	422021	0.1763	0.1925
Zr-As-O	1657243	0.1804	0.1918
Zr-P-O	65703	0.1754	0.1868
Zr-P-O	153124	0.1854	0.1763
Zr-As-O	1703454	0.1638	0.1746
Zr-P-O	250172	0.1433	0.1674
Th-As-O	238290	0.1266	0.1671
Th-As-O	1692456	0.0849	0.1617
Ce-As-O	54221	0.1370	0.1572
Ce-P-O	260053	0.0663	0.1544
Zr-P-O	428801	0.1145	0.1542
Ce-P-O	423035	0.0637	0.1507
Th-As-O	1684011	0.1594	0.1455
Ce-As-O	1733800	0.0610	0.1435
Ce-P-O	423884	0.0749	0.1417
Zr-P-O	150336	0.0686	0.1415
Ce-As-O	1739959	0.0550	0.1371
Ce-As-O	98207	0.1493	0.1365
Th-P-O	183574	0.1732	0.1330
Ce-As-O	54220	0.1040	0.1281
Ce-As-O	1697957	0.0415	0.1221
Zr-P-O	280395	0.1132	0.1217
Ce-As-O	291400	0.1773	0.1212
Ce-As-O	54219	0.0975	0.1154
Zr-As-O	1682802	0.1184	0.1150
Ce-As-O	1679122	0.0343	0.1133
Zr-P-O	4427	0.1294	0.1113
Zr-As-O	194801	0.0755	0.1111
Zr-As-O	1631503	0.1271	0.1095
Ce-As-O	181534	0.0130	0.1089
Zr-P-O	165330	0.1169	0.1062
Ce-As-O	1790812	0.0840	0.1062
Ce-P-O	262898	0.0780	0.1051
Zr-P-O	200017	0.1157	0.0984
Zr-As-O	183822	0.0707	0.0979
Ce-As-O	181535	0.0038	0.0978
Ce-As-O	54216	0.0862	0.0953
Ce-As-O	181536	-0.0033	0.0894
Ce-As-O	418025	0.0746	0.0850
Ce-As-O	181537	-0.0036	0.0820
Zr-P-O	428800	0.0485	0.0807

Zr-P-O	150877	0.0508	0.0798
Ce-As-O	418026	0.0752	0.0779
Zr-As-O	1699593	0.0393	0.0777
Zr-As-O	194799	0.0446	0.0654
Ce-P-O	425401	0.1272	0.0620
Ce-As-O	162820	-0.0122	0.0601
Th-As-O	1692454	0.0043	0.0576
Ce-As-O	162821	-0.0149	0.0571
Ce-As-O	162822	-0.0158	0.0558
Zr-As-O	194797	0.0614	0.0557
Zr-P-O	261232	0.0511	0.0545
Ce-As-O	181533	-0.0218	0.0526
Th-P-O	421965	0.0789	0.0498
Ce-As-O	168127	0.0764	0.0492
Zr-P-O	80390	0.0546	0.0484
Ce-As-O	162823	-0.0235	0.0471
Ce-As-O	406326	0.0654	0.0468
Zr-As-O	1647616	0.0592	0.0444
Zr-As-O	1699591	0.0765	0.0439
Zr-P-O	434046	0.0438	0.0427
Ce-As-O	162824	-0.0284	0.0413
Zr-P-O	173888	0.0574	0.0390
Zr-As-O	1647332	0.0398	0.0387
Ce-P-O	27859	0.0382	0.0372
Ce-P-O	76608	0.0582	0.0341
Th-As-O	1643419	-0.0312	0.0330
Ce-As-O	180544	-0.0203	0.0304
Ce-P-O	240880	0.0217	0.0298
Ce-As-O	3474	0.0449	0.0284
Zr-P-O	91112	0.0288	0.0222
Ce-P-O	160452	0.0432	0.0221
Ce-As-O	1623143	-0.0115	0.0184
Zr-As-O	190657	-0.0227	0.0172
Th-As-O	1717089	0.0067	0.0166
Ce-As-O	162818	-0.0500	0.0165
Zr-P-O	250163	0.0676	0.0148
Ce-As-O	160431	0.0114	0.0129
Ce-As-O	180543	0.0295	0.0119
Ce-P-O	41560	-0.0207	0.0103
Th-As-O	1599350	0.0134	0.0089
Zr-P-O	173842	0.0102	0.0077
Zr-P-O	424518	0.0322	0.0058
Ce-As-O	259107	0.0068	0.0057
Ce-P-O	244036	0.0000	0.0042
Ce-As-O	31255	0.0052	0.0039
Zr-P-O	201970	0.0041	0.0017
Zr-P-O	76021	-0.0043	-0.0047
Zr-P-O	424513	0.0134	-0.0132
Ce-As-O	413923	-0.0065	-0.0135

Th-P-O	246234	0.0398	-0.0136
Th-P-O	429057	-0.0467	-0.0190
Zr-As-O	281329	0.0094	-0.0224
Zr-As-O	190655	-0.0310	-0.0261
Ce-As-O	195618	-0.0469	-0.0464
Ce-As-O	55856	-0.0907	-0.0481
Ce-As-O	180542	-0.1101	-0.0594
Zr-P-O	62973	-0.0385	-0.0660
Ce-As-O	170470	-0.0967	-0.0771
Zr-As-O	268044	-0.0617	-0.0778
Ce-As-O	737292	-0.0879	-0.0968
Zr-P-O	201935	-0.1000	-0.1069
Zr-P-O	23014	-0.1036	-0.1127
Zr-P-O	24853	-0.1211	-0.1146
Ce-P-O	80808	-0.0550	-0.1240
Zr-P-O	246397	-0.1662	-0.1650
Zr-P-O	1281	-0.1268	-0.1669
Ce-As-O	417528	-0.1649	-0.1830
Zr-P-O	172200	-0.1721	-0.1856
Ce-As-O	16903	-0.2536	-0.1926
Zr-As-O	1596689	-0.1802	-0.2168
Zr-P-O	81484	-0.2012	-0.2185
Ce-As-O	107652	-0.2620	-0.2304
Ce-As-O	107653	-0.2609	-0.2316

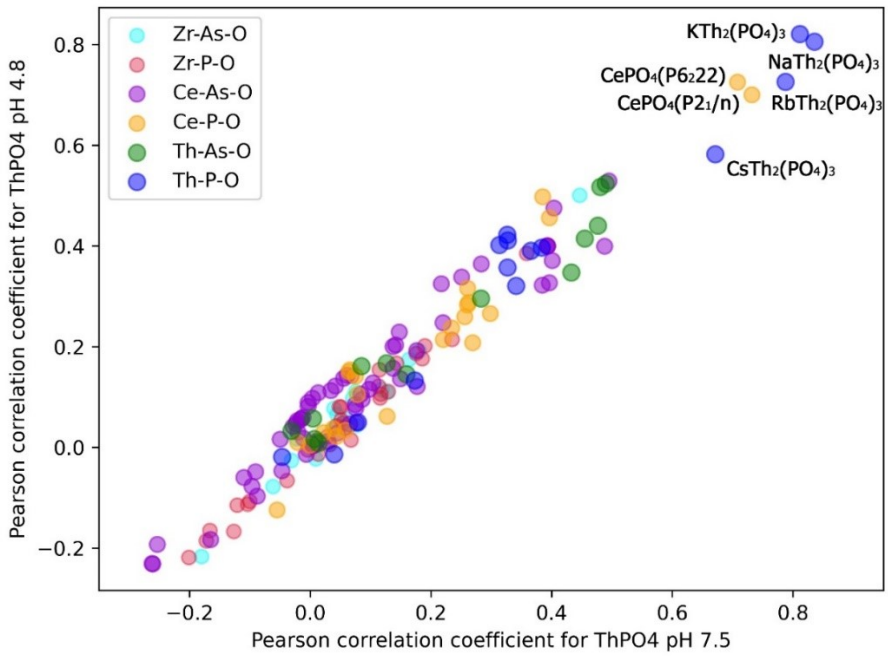

Figure S14. Pearson correlation coefficients (r) from and synchrotron-based PDFs for ThPhos-5 and ThPhos-8 compared with calculated PDFs of Zr-P-O (red), Zr-As-O (sky blue), Ce-P-O (yellow), Ce-As-O (purple), Th-P-O (blue), Th-As-O (green) compounds. The highest correlation coefficients between experimental data and calculated PDFs were found for the $NaTh_2(PO_4)_3$ and $KTh_2(PO_4)_3$ structures (ICSD numbers are 1536395 and 30432, respectively).

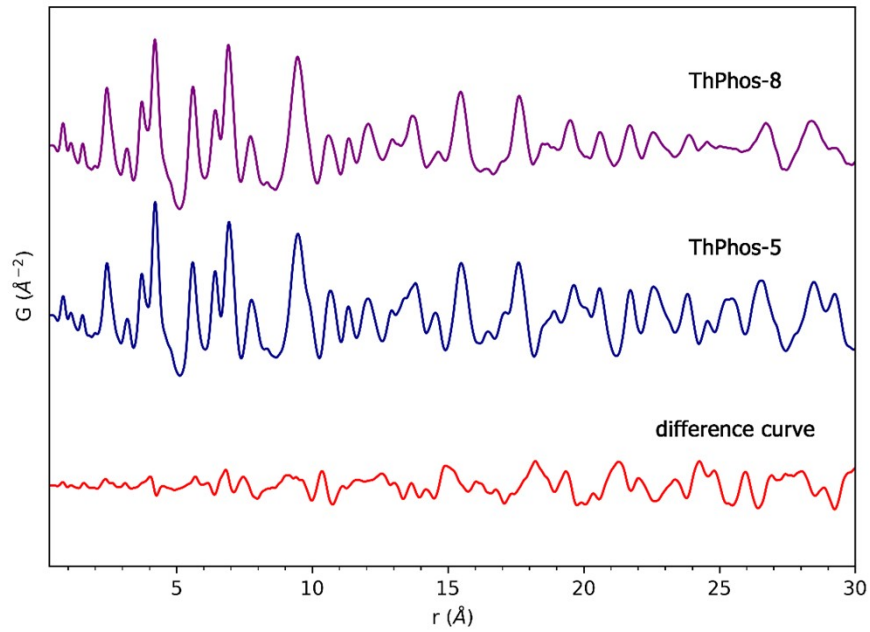

Figure S15. Experimental PDF for ThPhos-5 (purple curve), ThPhos-8 (blue curve), and their difference curve (red curve).

Section S9. Addendum to EXAFS analysis

Quantitative EXAFS analysis was performed using curve fitting to theoretical standards with the Demeter software suite, which incorporates FEFF. The overall number of parameters used for analysis varied from sample to sample, adhering to the Nyquist criterion. The k-space data was windowed with the Hann function prior to Fourier transform. The amplitude reduction factor S_0^2 for samples ThPhos-5 and ThPhos-8 was determined to be about 0.997 (~1) by fitting a reference sample of crystalline thorium dioxide measured on the same beamline. For consistency, the amplitude reduction factor for samples ThPhos-5-1000 and ThPhos-8-1000 (which were measured at a later date) was set to 1. The feature at R = 1.3 in the Fourier transform magnitude stems from the multielectron excitation;[11] it does not affect the results of the analysis. The fitting window was constrained to a minimal R = 1.5 Å.

The wavelet transform was performed with the aid of the **pycwt** Python package. Morlet wavelet was chosen as the mother wavelet.

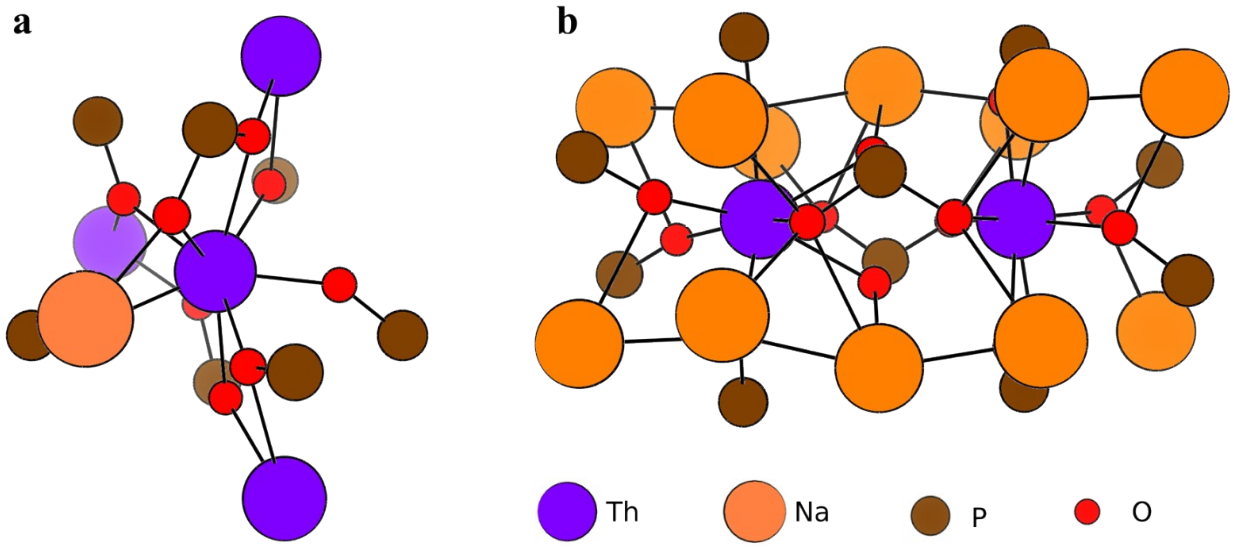

Figure S16. The models used for EXAFS fitting, based on the published structures for (a) $NaTh_2(PO_4)_3$ and (b) $Na_2Th(PO_4)_2$. For clarity, only atoms as far as two bonds away from a thorium absorber are shown.

In the figures below, the Morlet wavelet transform of the k^3-weighted EXAFS spectra for samples ThPhos-5-1000 and ThPhos-8-1000 is performed with the central frequency corresponding to either a half path length of 2 Å (Fig. SX a,c) or a half path length of 5 Å (Fig. SX b,d). (This means that the actual central Morlet frequency is set to the half path length multiplied by two). Best resolution for specific paths is achieved when the central frequency matches the physical half-path length; otherwise, distortion in the k- or R-direction is observed. Setting central frequency corresponding to 2 Å allows k-R

localization of the Th—O paths at k ~ 5.2, R ~ 2.2. The residual intensity at k ~ 10.1, R ~2.2 likely corresponds to a multiple scattering path or stems from interference of multiple close-lying paths. The long half-path length of 5 Å improves resolution for the longer paths (Th—Th in ThPhos-5-1000, Th—Na and Th—Th in ThPhos-8-1000).

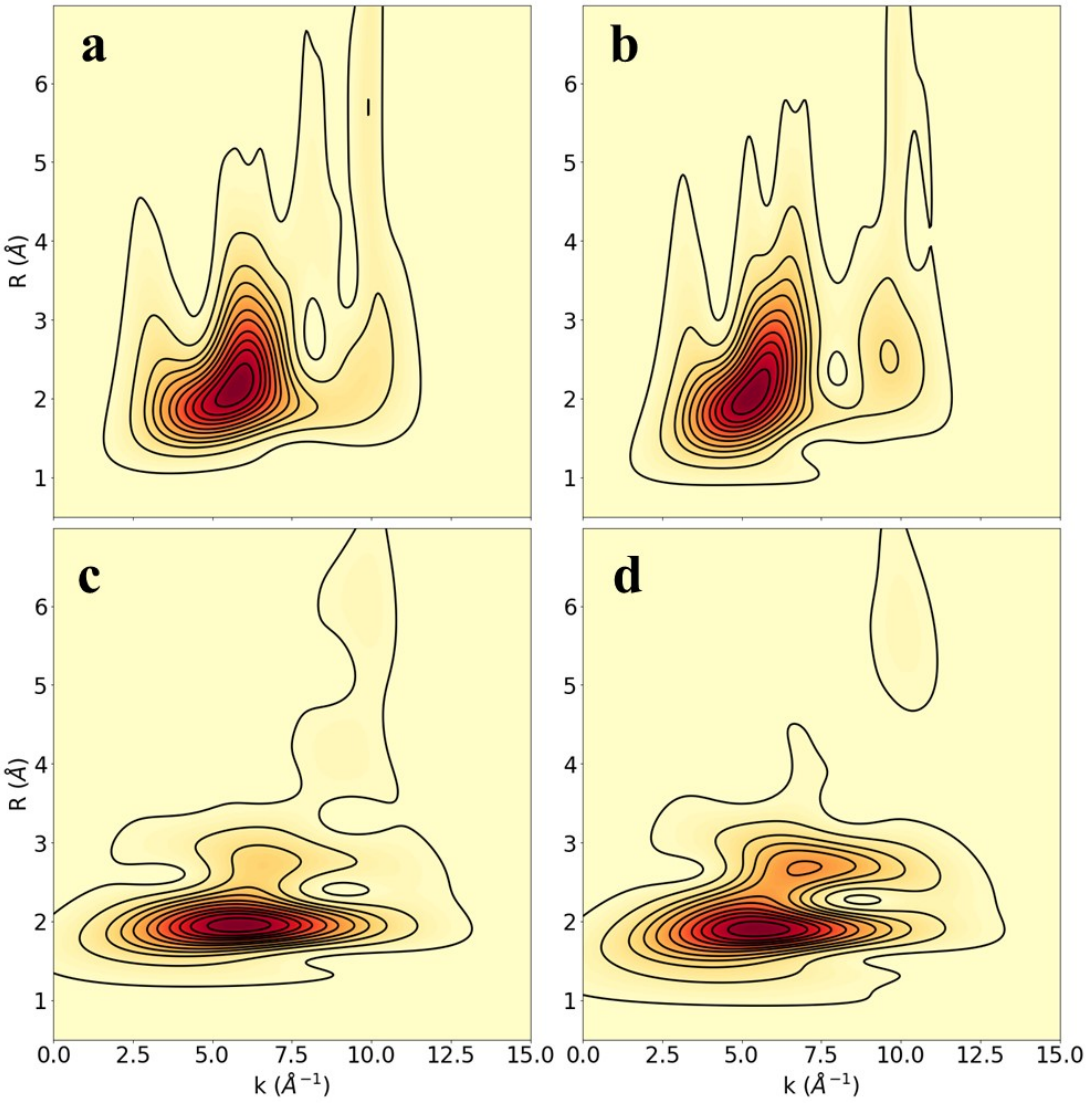

Figure S17. WT-EXAFS visualized for samples ThPhos-5-1000 and ThPhos-8-1000 for a half path length of 2 Å (a,c) or 5 Å (b,d).

Section S10. Full EXAFS Fitting Parameters

The parameters for multiple scattering paths were constrained by the corresponding single scattering path parameters so as to not introduce any new ones. The Nyquist criterion was adhered to at all times. Fitting was carried out in k^3, k^2 and k weights simultaneously. R_{bkg} was set to about 1.2, justified by the large first-shell Th—O distances around 2.4 Å. No cumulant parameters were utilized in fitting any of the four EXAFS datasets. The coordination numbers for the oxygen atoms in the first shell were fixed based on fit quality and the assumption that the total number of Th-O bonds equals 9 (or 8 for ThPhos-8-1000/$Na_2Th(PO_4)$). The Th—Th coordination number was fixed based on what motif the samples were assigned to, $NaTh_2(PO_4)_3$ or $Na_2Th(PO_4)$, see main text. No conclusions are made from the split in the Th-O paths, because the differences in their bond length are at the limit which EXAFS can resolve with the k-range available here. Debye-Waller parameters were generally shared based on atomic number. Multiple scattering paths, when used, did not have a significant effect on the fit quality.

Table S10. Full fitting parameters for samples ThPhos-5 and ThPhos-8.

	Path	N	σ^2	ΔR	$R_{cryst.}$	R
ThPhos-5	$O_{1,1}$	**3.0**	0.002 ± 0.003[a]	-0.036 ± 0.021	**2.379**	2.343 ± 0.021
	$O_{1,2}$	**4.0**	0.002 ± 0.003[a]	-0.004 ± 0.027	**2.471**	2.468 ± 0.027
	$O_{1,3}$	**2.0**	0.002 ± 0.003[a]	-0.028 ± 0.048	**2.628**	2.600 ± 0.048
	P_2	3.3 ± 1.9	0.008 ± 0.006[b]	0.107 ± 0.030	**3.131**	3.239 ± 0.030
	O_1P_2	8.7 ± 3.9	0.010 ± 0.010	0.039 ± 0.086	**3.627**	3.666 ± 0.086
	P_3	3.7 ± 1.6	0.008 ± 0.006[b]	0.085 ± 0.037	**3.696**	3.780 ± 0.037
	Th_4	**3.0**	0.020 ± 0.001	0.282 ± 0.155	**4.267**	4.549 ± 0.155
ThPhos-8	$O_{1,1}$	**3.0**	0.004 ± 0.006[a]	-0.065 ± 0.032	**2.379**	2.314 ± 0.032
	$O_{1,2}$	**5.0**	0.004 ± 0.006[a]	-0.015 ± 0.024	**2.471**	2.457 ± 0.024
	$O_{1,3}$	**1.0**	0.004 ± 0.006[a]	-0.015 ± 0.105	**2.628**	2.613 ± 0.105
	P_2	1.9 ± 0.6	0.004 ± 0.003[b]	0.075 ± 0.018	**3.131**	3.206 ± 0.018
	O_1P_2	5.1 ± 1.3	0.008 ± 0.009	0.023 ± 0.123	**3.627**	3.650 ± 0.123
	P_3	2.5 ± 0.8	0.004 ± 0.003[b]	0.068 ± 0.024	**3.696**	3.763 ± 0.024
	Th_4	**3.0**	0.020 ± 0.001	0.211 ± 0.107	**4.267**	4.479 ± 0.107

*[a,b]Parameters shared between multiple paths. Fixed parameters denoted in **bold.** Multiple scattering paths had their ΔR and σ^2 parameters tied to those of the corresponding single scattering paths.*

$S_0^2 = 0.997$.

$R_{cryst.}$ refers to the corresponding bond length in the crystal structure of $NaTh_2(PO_4)_3$.

The index values in atom labels indicate scattering shell assignment.

Table S11. Full fitting parameters for samples ThPhos-5-1000 and ThPhos-8-1000.

	Path	N	σ^2	ΔR	$R_{cryst.}$	R
ThPhos-5-1000	$O_{1,1}$	**5.0**	0.003 ± 0.001[a]	0.027 ± 0.010[a]	**2.379**	2.407 ± 0.010[a]
	$O_{1,2}$	**3.0**	0.003 ± 0.001[a]	0.027 ± 0.010[a]	**2.518**	2.546 ± 0.010[a]
	$O_{1,3}$	**1.0**	0.003 ± 0.001[a]	0.027 ± 0.010[a]	**2.628**	2.655 ± 0.010[a]
	P_2	3.4 ± 1.3	0.008 ± 0.004[b]	0.110 ± 0.016	**3.131**	3.242 ± 0.016
	O_1P_2	6.7 ± 2.6	0.011 ± 0.005	0.138 ± 0.026	**3.627**	3.765 ± 0.026
	P_3	2.0 ± 1.0	0.008 ± 0.004[b]	0.201 ± 0.038	**3.582**	3.782 ± 0.038
	Th_4	**3.0**	0.011 ± 0.005	0.090 ± 0.042	**4.130**	4.220 ± 0.042
ThPhos-8-1000	$O_{1,1}$	**3.0**	0.005 ± 0.001[a]	0.014 ± 0.007[a]	**2.365**	2.379 ± 0.007[a]
	$O_{1,2}$	**2.0**	0.005 ± 0.001[a]	0.014 ± 0.007[a]	**2.366**	2.380 ± 0.007[a]
	$O_{1,3}$	**1.0**	0.005 ± 0.001[a]	0.014 ± 0.007[a]	**2.506**	2.519 ± 0.007[a]
	$O_{1,4}$	**2.0**	0.005 ± 0.001[a]	0.014 ± 0.007[a]	**2.562**	2.576 ± 0.007[a]
	$O_{2,1}$	**1.0**	0.005 ± 0.001[a]	0.027 ± 0.007	**2.971**	2.998 ± 0.007[a]
	P_2	3.7 ± 1.4	0.005 ± 0.003[b]	0.074 ± 0.029	**3.138**	3.212 ± 0.029
	$O_{2,2}$	**1.0**	0.005 ± 0.001	0.027 ± 0.090	**3.361**	3.388 ± 0.090
	P_3	2.7 ± 0.8	0.005 ± 0.003[b]	0.103 ± 0.019	**3.629**	3.732 ± 0.019
	$Na_{4,1}$	4.6 ± 2.6	0.007 ± 0.006[c]	0.106 ± 0.024	**3.911**	4.018 ± 0.024
	$Na_{4,2}$	5.5 ± 3.4	0.007 ± 0.006[c]	0.160 ± 0.030	**4.125**	4.284 ± 0.030
	Th_5	**1.0**	0.005 ± 0.004	0.106 ± 0.038	**4.820**	4.926 ± 0.038

*[a,b,c]Parameters shared between multiple paths. Fixed parameters denoted in **bold.** Multiple scattering paths had their ΔR and σ^2 parameters tied to those of the corresponding single scattering paths.*

S_0^2 was set to 1.0 (data was collected separately from the ThPhos-5 and ThPhos-8 samples).

$R_{cryst.}$ refers to the corresponding path length in the reference crystal structure ($NaTh_2(PO_4)_3$ for ThPhos-5-1000, $Na_2Th(PO_4)_2$ for ThPhos-8-1000).

The index values in atom labels indicate scattering shell assignment.

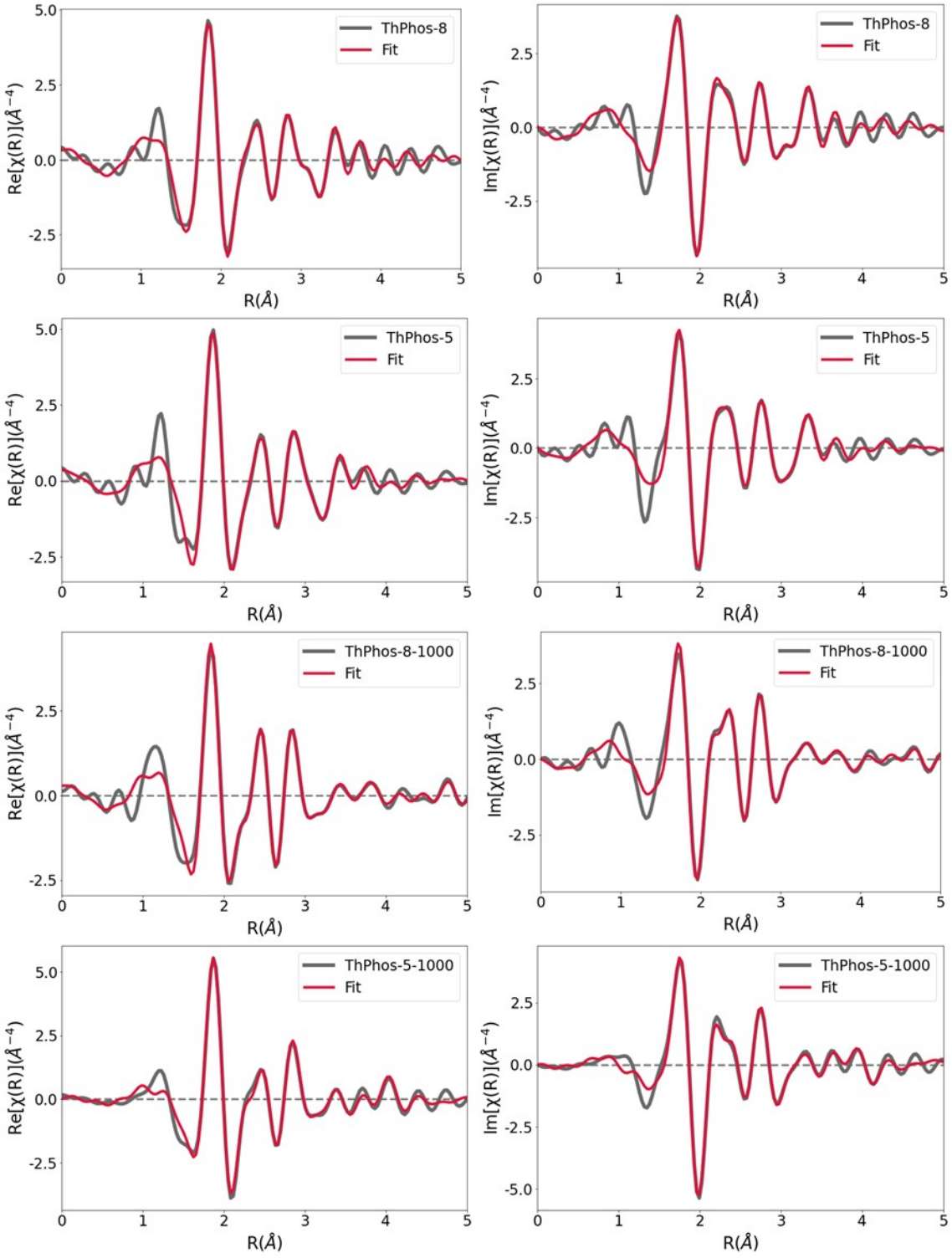

Figure S18. EXAFS Fitting: real (left column) and imaginary (right column) parts.

Section S11. X-ray absorption near edge structure

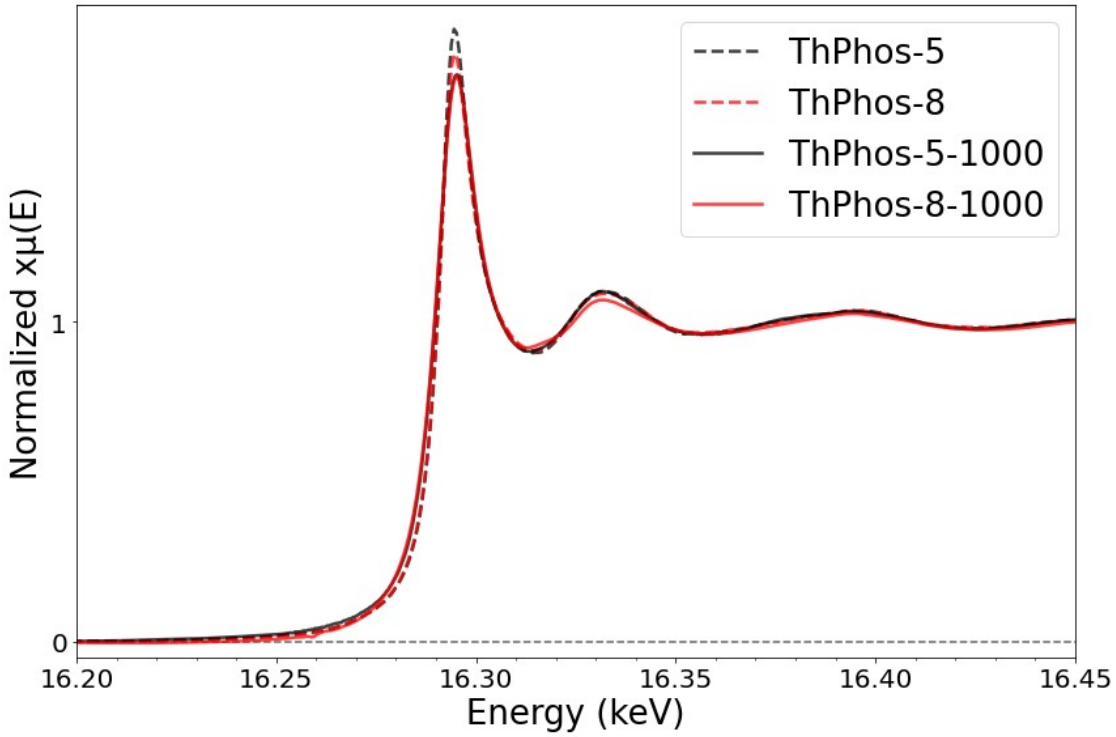

Figure S19. XANES for all four samples studied: ThPhos-5 in dashed, black; ThPhos-8 in dashed, red; ThPhos-5-1000 in solid black; and ThPhos-8-1000 in solid red.

Section S12. MAS-NMR

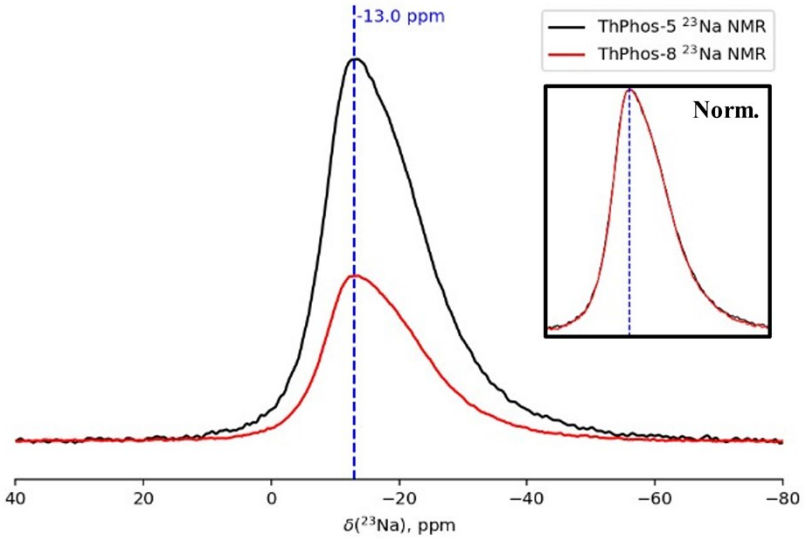

Figure S20. ^{23}Na MAS-NMR spectra of ThPhos-5 (black) and ThPhos-8 (red). Inset: normalized.

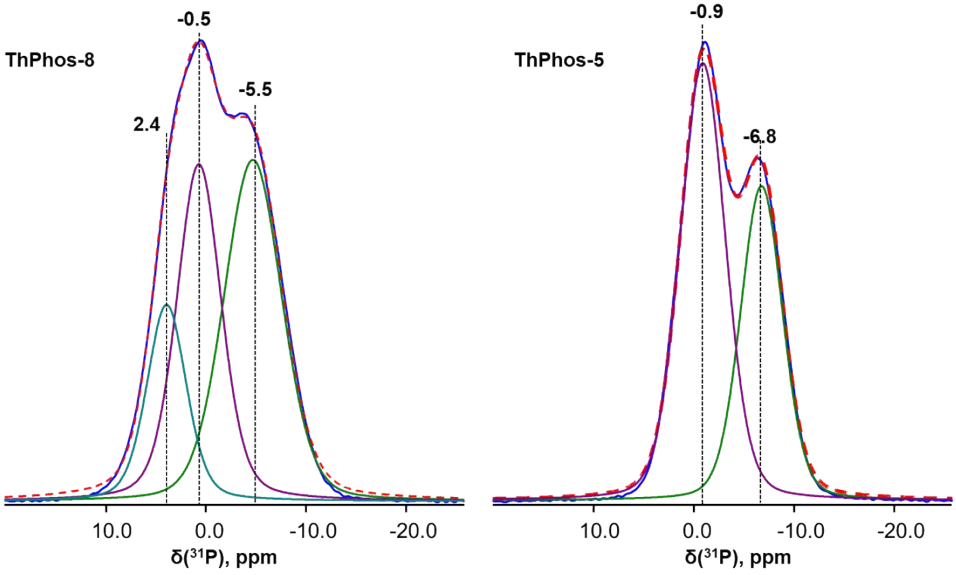

Figure S21. Spectral component decomposition for the ^{31}P NMR spectra of samples ThPhos-8 (left) and ThPhos-5 (right).

Table S12. Chemical shifts and molar site densities for the components in Fig. S20.

	ThPhos-8			ThPhos-5	
c.s., ppm	**2.4**	**-0.5**	**-5.3**	**-0.9**	**-6.8**
sites, mmol/g	0.7	1.4	1.8	1.7	2.5

References

1 V. B. Kalinin, A. M. Golubev, V. A. Tafeenko and S. Yu. Stefanevich, Crystal structure and phase transitions in $NaTh_2(PO_4)_3$, *Kristallografiya*, 1992, **37**, 1220–1226.

2 N. Galešić, B. Matković, M. Topić, E. Coffou and M. Šljukić, The Crystal Structure of Disodium Thorium Bisphosphate, $Na_2Th(PO_4)_2$, *Croatica Chemica Acta*, 1984, **57**, 597–608.

3 J. Alamo and R. Roy, Crystal chemistry of the $NaZr_2(PO_4)_3$, NZP or CTP, structure family, *Journal of Materials Science*, 1986, **21**, 444–450.

4 G. Wallez, N. Clavier, N. Dacheux, M. Quarton and W. van Beek, From thorium phosphate hydrogenphosphate hydrate to *β*-thorium phosphate diphosphate: Structural evolution to a radwaste storage ceramic, *Journal of Solid State Chemistry*, 2006, **179**, 3007–3016.

5 F. Hund and W. Dürrwächter, Anomale Mischkristalle im System ThO_2–La_2O_3, *Zeitschrift für anorganische und allgemeine Chemie*, 1951, **265**, 67–72.

6 E. Lissel, M. Jansen, E. Jansen and G. Will, Bestimmung der Kristallstruktur von T-Na_3PO_4 mit Röntgen- und Neutronenpulvertechniken, *Zeitschrift für Kristallographie*, 1990, **192**, 233–243.

7 G. Beaucage, Approximations Leading to a Unified Exponential/Power-Law Approach to Small-Angle Scattering, *Journal of Applied Crystallography*, 1995, **28**, 717–728.

8 B. Hammouda, Analysis of the Beaucage model, *J Appl Cryst*, 2010, **43**, 1474–1478.

9 B. Hammouda, A new Guinier–Porod model, *J Appl Cryst*, 2010, **43**, 716–719.

10 G. P. Shrivastav, V. Banerjee and S. Puri, Non-Porod behavior in systems with rough morphologies, *Eur. Phys. J. E*, 2014, **37**, 98.

11 C. Hennig, Evidence for double-electron excitations in the L_3-edge x-ray absorption spectra of actinides, *Phys. Rev. B*, 2007, **75**, 035120.